Available online at www.sciencedirect.com
SCIENCE DIRECT®
Journal of Computational Physics 201 (2004) 286–314
JOURNAL OF COMPUTATIONAL PHYSICS
www.elsevier.com/locate/jcp

Spectral element methods for transient viscoelastic flow problems

R.G.M. van Os, T.N. Phillips *

Department of Mathematics, University of Wales, Aberystwyth SY23 3BZ, UK

Received 27 June 2003; received in revised form 24 May 2004; accepted 27 May 2004
Available online 8 July 2004

Abstract

Spectral element methods are developed for solving transient flows of viscoelastic fluids. The fluids are modeled using the upper-convected Maxwell and Oldroyd B constitutive relationships. Several temporal schemes for dealing with the time dependent nature of the problems are considered. The computation associated with each time step comprises an explicit treatment of the convection and deformation terms and an implicit treatment of the linear terms. The generalized three field Stokes problem generated in the latter is solved using a nested preconditioned conjugate gradient method. The performance of a number of preconditioners is investigated. A modified formulation of the Stokes problem is presented that ensures a unique pressure approximation with zero mean is obtained at each time step. The performance of the schemes and models when applied to the benchmark problem of start-up of plane Poiseuille flow is investigated.

Keywords: Transient flow; Poiseuille; Viscoelastic fluid; Oldroyd B

1. Introduction

Viscoelastic fluids are examples of a broader class of fluids called non-Newtonian fluids. Newtonian fluids are characterized by the assumption that the extra-stress tensor is a linear isotropic function of the components of the velocity gradient. In the case of an incompressible fluid this leads to the Navier–Stokes equations. One can then define a non-Newtonian fluid as one whose behaviour cannot be described on the basis of the Navier–Stokes equations. Non-Newtonian fluids abound in nature and industry and this accounts for the interest in their flow properties and behaviour.

The governing equations resulting from a macroscopic description of a viscoelastic fluid comprise the conservation equations of mass and momentum together with a differential or integral constitutive equation

* Corresponding author. Tel.: +44-1970-622769; fax: +44-1970-622777.
E-mail addresses: rgv01@aber.ac.uk (R.G.M. van Os), tnp@aber.ac.uk (T.N. Phillips).

0021-9991/$ - see front matter © 2004 Elsevier Inc. All rights reserved.
doi:10.1016/j.jcp.2004.05.016

relating the stress to the strain. Differential constitutive models such as the upper-convected Maxwell (UCM), Oldroyd B and Phan-Thien/Tanner models, for example, are nonlinear and this property has a considerable impact on the performance and stability of numerical methods. The degree of nonlinearity of the governing system of partial differential equations may be quantified in terms of a dimensionless number, We, known as the Weissenberg number which can be viewed as a measure of the memory of the fluid. Most numerical algorithms fail to converge above a critical value of this parameter when conventional closed form constitutive models such as the UCM or Oldroyd B models, for example, are used.

Over the last 20 years significant progress has been made in the development of reliable numerical methods for solving steady viscoelastic flow problems (see the monograph of Owens and Phillips [24], for example). On a range of benchmark problems there has been agreement across a range of numerical methods for particular models in terms of global quantities such as the drag on a sphere or cylinder in a viscoelastic medium. Stabilization techniques have been used to remove numerical instabilities in many instances in order to extend the range of Weissenberg numbers over which converged numerical solutions are obtained. One such technique is the elastic viscous split stress (EVSS) formulation, developed by Perera and Walters [25], in which a change of variables is introduced with the purpose of increasing the 'ellipticity' of the momentum equation and, therefore, the stability of the discretization. Other successful stabilization techniques are described in Owens and Phillips [24]. These methods have been shown to work well for steady problems. However, they may pollute the accuracy of the transient solution to unsteady problems and for this reason they are not used in the present study.

In the context of spectral methods, Fiétier and Deville [8] have explored the use of stabilization techniques such as the discrete EVSS (DEVSS) method of Guénette and Fortin [13] and the filtering method of Mullen and Fischer [23]. However, these techniques only had limited success in increasing the critical value of We. Furthermore, the authors were concerned that the use of stabilization techniques could prevent a detailed investigation into the onset and development of physical instabilities that are observed experimentally (see Smith et al. [31], for example).

Much theoretical and numerical work has been performed with respect to the flow of UCM and Oldroyd B fluids in a planar channel. In the 1970s, Porteous and Denn [26], Ho and Denn [14] and later Lee and Finlayson [18] and Larson [17] performed linear stability analyses of this flow.

Porteous and Denn [26] performed a linear stability analysis of the plane Poiseuille flow of a UCM fluid at high Reynolds numbers. Their calculations showed that with increasing fluid elasticity there is a sharp decrease in the Reynolds number at which fully-developed laminar flow breaks down. Thus, elasticity is destabilizing in the inertial regime. However, in the low Reynolds number regime the linear stability analysis of Ho and Denn [14] has shown that this flow is stable to infinitesimal perturbations. Thus, in the creeping flow limit the UCM fluid is linearly stable.

In a more recent paper Sureshkumar and Beris [32] used an Arnoldi algorithm, which computes a group of the most unstable eigenmodes, to show that the addition of solvent viscosity considerably reduced the destabilizing effect of elasticity found by Porteous and Denn [26] for the UCM fluid in the inertial regime. They also commented on the dire consequences of inadequately resolving the continuous eigenmodes. For a given mesh the error in the approximation of these eigenmodes was shown to increase linearly with the Weissenberg number. Therefore, at relatively large values of We these modes could give rise to artificial instabilities if insufficient spatial refinement is used in the computations.

Wilson et al. [34] studied the structure of the spectrum for creeping flow of both UCM and Oldroyd B fluids. The addition of solvent viscosity is found to increase the complexity of the eigenspectrum. Although the authors were not able to prove that inertialess plane Poiseuille flow is linearly stable for all values of the Weissenberg number, no unstable eigenvalues were observed. However, poorly resolved modes of the continuous spectrum can produce spurious instabilities. The problem of under-resolution of the continuous part of the spectrum for UCM and Oldroyd B models and its impact on the generation of spurious instabilites for plane Couette flow was studied by Keiller [16]. He showed that, since the continuous part of

the spectrum scales linearly with both wavenumber k_x and the order of the spectral approximation N, the critical Weissenberg number will scale with the aspect ratio of the mesh elements k_x/N when the under-resolved part of the continuous spectrum is causing the flow to appear unstable. He also showed that for calculations with the UCM model, the addition of a small amount of solvent viscosity could stabilize the spurious modes.

Atalik and Keunings [1] performed a nonlinear analysis of the evolution of two-dimensional disturbances for plane Poiseuille flow of the Giesekus fluid, which includes the UCM and Oldroyd B fluids as special cases, in the low and high Reynolds number regimes. The numerical scheme of Atalik and Keunings is based on a spectral discretization in space and a Crank–Nicolson/Adams–Bashforth discretization in time. The authors noted that the linear operator describing the time evolution of infinitesimal disturbances is non-normal for this problem. Thus, although all the eigenvalues of the two-dimensional linear operator have negative real parts, so that any infinitesimal disturbance will ultimately decay, transient growth of the disturbances is possible. If the intermediate growth is significant enough the disturbances that are misfit to the eigendirections of the linear stability operator will interact in a nonlinear fashion and eventually drive the system to a nonlinear instability. In the inertial regime they showed that finite amplitude periodic waves develop beyond a critical Reynolds number. Increasing the elasticity number has a destabilizing effect at first followed by restabilization. For Reynolds numbers of the order of 10^{-1} they showed that two-dimensional finite amplitude disturbances appear to decay when the ratio of retardation to relaxation times for an Oldroyd B fluid exceeds 10^{-2} but that for smaller values of this ratio finite amplitude waves can develop.

Other pertinent issues such as the mathematical type of the equations, loss of evolution and the high Weissenberg number problem, for example, are discussed in Owens and Phillips [24], Renardy et al. [27] and Renardy [28–30]. More recently, Lozinski and Owens [19] have derived an energy estimate for the velocity and stress components for both inertial and creeping flows of an Oldroyd B fluid. They explained that conventional discretization schemes for the Oldroyd B model may violate the energy estimate and deliver an approximation that fails to respect important properties of the continuous problem. A novel numerical scheme that respects the energy estimate and guarantees satisfaction of key properties of the model was developed and implemented by the authors.

In the analysis of the standard weak formulation of the Stokes problem defined in some bounded domain Ω it can be shown that a unique pressure solution exists in $L^2_0(\Omega)$, the subspace of $L^2(\Omega)$ containing functions with zero mean value. To construct a conforming discrete pressure space one would need to ensure that all the trial and test functions individually satisfy the zero volume condition. This is not done in practice due to the constraints of the interpolants that must be imposed. In this paper, an alternative formulation of the Stokes problem is presented that does not require the pressure to belong to $L^2_0(\Omega)$. The continuity equation is suitably modified by adding a multiple of the mean value of the pressure to the right-hand side. One can then show that there exists a unique pressure solution to this problem in $L^2(\Omega)$ and that this solution possesses a zero mean value over Ω. The alternative formulation also results in a better conditioned Uzawa operator. In fact, the operator is positive definite whereas it is positive semi-definite in the standard formulation. Obviously, this has important consequences for its inversion using iterative methods.

The paper is organized as follows. In Section 2 the governing equations for an Oldroyd B fluid are presented. The transient analytical solution for Poiseuille flow in a planar channel is given in Section 3. The transient discretization of the governing equations is considered in Section 4 and the semi-discrete equations are derived. The spatial discretization is described in Section 5 and important features of the spectral element method are introduced. The application of the conjugate gradient method to solve the discrete equations at each time step and the performance of a number of preconditioners are also described in Section 5. Numerical results are presented and discussed in Section 6 before concluding remarks are made in Section 7.

2. Governing equations

The equations governing the flow of an Oldroyd B fluid comprise the field equations, or conservation equations of mass and momentum, and a rheological equation of state, or constitutive equation, relating the stress and strain. The constitutive equation for an Oldroyd B fluid is nonlinear which means that, unlike the corresponding situation for a Newtonian fluid, the stress cannot be eliminated from the system of equations. Therefore, one has to solve for the extra-stress tensor in addition to the velocity and pressure.

The first field equation is the mathematical statement of the conservation of mass for an incompressible fluid. It is given by

$$\nabla \cdot \mathbf{u} = 0. \tag{1}$$

The second field equation is the mathematical statement of the conservation of momentum and reads

$$\rho\left(\frac{\partial \mathbf{u}}{\partial t} + \mathbf{u} \cdot \nabla \mathbf{u}\right) = -\nabla p + \nabla \cdot \mathbf{T}, \tag{2}$$

where ρ is the density of the fluid, p is the pressure, and $\mathbf{T}$ is the extra-stress tensor. The contents of the bracket on the left-hand side of (2) are known as the material derivative of $\mathbf{u}$. When inertia is neglected, the material derivative is set to zero, and the Navier–Stokes equations reduce to the Stokes equations. To relate the extra-stress tensor to the rate-of-deformation tensor, a constitutive equation is needed. In the Navier–Stokes and the Stokes equations, the constitutive equation is the Newtonian stress relation

$$\mathbf{T} = 2\eta\mathbf{d}, \tag{3}$$

where η is the viscosity and $\mathbf{d}$ is the rate-of-deformation tensor, given by

$$\mathbf{d} = \tfrac{1}{2}(\nabla \mathbf{u} + (\nabla \mathbf{u})^{\mathrm{T}}). \tag{4}$$

Note that, in the above system of equations, pressure is determined up to an arbitrary constant.

2.1. The Oldroyd B constitutive model

For viscoelastic fluids, the linear stress relation (3) is no longer valid. The simplest model, in terms of mathematical complexity, is the UCM model, in which the relation between the extra-stress tensor and the rate-of-deformation tensor, is given by

$$\mathbf{T} + \lambda_1 \overset{\nabla}{\mathbf{T}} = 2\eta\mathbf{d}. \tag{5}$$

In this equation, λ_1 is the relaxation time of the fluid, and $\overset{\nabla}{\mathbf{T}}$ is the upper convected derivative of the extra-stress tensor, defined by

$$\overset{\nabla}{\mathbf{T}} = \frac{\partial \mathbf{T}}{\partial t} + (\mathbf{u} \cdot \nabla)\mathbf{T} - \nabla \mathbf{u} \cdot \mathbf{T} - \mathbf{T} \cdot (\nabla \mathbf{u})^{\mathrm{T}}. \tag{6}$$

The first two terms in (6) comprise the material derivative of the extra-stress tensor. The two other terms in Eq. (6) are the deformation terms. The presence of these terms ensures that the principle of coordinate invariance holds, i.e., the relationship between the stress tensor and the deformation history does not depend on the particular coordinate system used for the description.

The nonlinear upper-convected derivative introduces a hyperbolic component to the set of equations. The governing set of partial differential equations for a UCM fluid is of mixed hyperbolic/elliptic type. At

high Weissenberg numbers, the nonlinear upper-convected derivative becomes dominant. This hyperbolic part of the equations gives rise to mathematical and numerical problems. Numerical techniques can be applied to stabilize the UCM model. In this paper, none of these techniques are adopted.

In the case of the Oldroyd B model a decomposition of the extra-stress tensor into solvent and polymeric parts introduces a diffusion term into the momentum equation. This decomposition has a stabilizing influence on the performance of numerical discretization schemes. The Oldroyd B model is given by

$$\mathbf{T} + \lambda_1 \overset{\nabla}{\mathbf{T}} = 2\eta(\mathbf{d} + \lambda_2 \overset{\nabla}{\mathbf{d}}). \tag{7}$$

The retardation time λ_2 may be seen as a measure of the time the material needs to respond to deformation. The extra-stress tensor can be written in terms of polymeric and viscous contributions as follows:

$$\mathbf{T} = \boldsymbol{\tau} + 2\eta_2 \mathbf{d}. \tag{8}$$

The viscosity may be expressed as a sum of its polymeric contribution η_1, and its viscous contribution η_2. The retardation and relaxation times, and the viscosity contributions are related through

$$\frac{\lambda_2}{\lambda_1} = \frac{\eta_2}{\eta_1 + \eta_2}. \tag{9}$$

The equations can now be rewritten in terms of the polymeric contribution to the extra-stress tensor. The conservation of mass and momentum, and the constitutive equation now read:

$$\nabla \cdot \mathbf{u} = 0, \tag{10}$$

$$\rho\left(\frac{\partial \mathbf{u}}{\partial t} + \mathbf{u} \cdot \nabla \mathbf{u}\right) = -\nabla p + \nabla \cdot \boldsymbol{\tau} + \eta_2 \nabla^2 \mathbf{u}, \tag{11}$$

$$\boldsymbol{\tau} + \lambda_1 \overset{\nabla}{\boldsymbol{\tau}} = 2\eta_1 \mathbf{d}. \tag{12}$$

The Oldroyd B model reduces to the UCM model if λ_2 or, equivalently, η_2 is equal to zero. Both models predict a positive first normal stress difference and a zero second normal stress difference, which is in qualitative agreement with experimental data for Boger fluids [2]. However, they may both predict unbounded stress growth, as a result of the possibility of generating infinite extensional viscosity.

It can be shown that the stress tensor $\boldsymbol{\tau}_A = \boldsymbol{\tau} + (\eta_1/\lambda_1)\mathbf{I}$ is positive definite. This is an important property of the Oldroyd B model. The numerical scheme of Lozinski and Owens [19] ensures that the discrete analogue of this tensor preserves this property automatically.

2.2. Non-dimensional equations

In terms of non-dimensional variables, the governing set of equations for the Oldroyd B model becomes:

$$\nabla \cdot \mathbf{u} = 0, \tag{13}$$

$$Re\left(\frac{\partial \mathbf{u}}{\partial t} + \mathbf{u} \cdot \nabla \mathbf{u}\right) = -\nabla p + \nabla \cdot \boldsymbol{\tau} + \beta \nabla^2 \mathbf{u}, \tag{14}$$

$$\boldsymbol{\tau} + We \overset{\nabla}{\boldsymbol{\tau}} = 2(1 - \beta)\mathbf{d}. \tag{15}$$

The factor β, the Reynolds number and the Weissenberg number are given by

$$\beta = \frac{\lambda_2}{\lambda_1}, \quad Re = \frac{\rho UL}{\eta}, \quad We = \frac{\lambda_1 U}{L}, \tag{16}$$

where U and L denote a characteristic velocity and a characteristic length, respectively. When $\beta = 0$ (which implies $\lambda_2 = 0$), this set of equations reduces to the governing equations for the UCM model.

3. Poiseuille flow in a planar channel

The benchmark problem chosen in this study is plane Poiseuille flow in a channel bounded by two parallel fixed plates. This problem has been chosen since an analytical solution exists for both the steady and transient problems. This enables the accuracy as well as the stability of numerical schemes to be investigated.

The analytical solution for the flow of an Oldroyd B fluid in a planar channel (see Fig. 1) can easily be found at steady state. With all derivatives in the channel direction (x) set to zero, and the cross channel velocity $v = 0$, a parabolic velocity profile for the velocity component u, is obtained of the form

$$u(y) = A(y) = 4(1 - y)y. \tag{17}$$

This is valid in a channel of height $h = 1$ and $0 \leqslant y \leqslant h$, with a maximum centerline velocity of $U = 1$. The elastic stresses can now be found by solving the constitutive equation using the above assumptions. This yields:

$$\tau_{xx} = 2We(1 - \beta)\left(\frac{\partial u}{\partial y}\right)^2 = 2We(1 - \beta)(A'(y))^2, \tag{18}$$

$$\tau_{xy} = (1 - \beta)\left(\frac{\partial u}{\partial y}\right) = (1 - \beta)(A'(y)), \tag{19}$$

$$\tau_{yy} = 0. \tag{20}$$

With a constant pressure gradient applied, the analytical solution to the transient start-up of a channel flow of an Oldroyd B fluid has been derived by Waters and King [33] for $Re \neq 0$. The velocity components of this solution are given by:

$$u(y,t) = U\left[A(y) - 32\sum_{n=1}^{\infty}\frac{\sin(Ny)}{N^3}\exp\left(-\frac{\alpha_N t}{2S_1}\right)G_N(t)\right], \tag{21}$$

$$v(y,t) = 0, \tag{22}$$

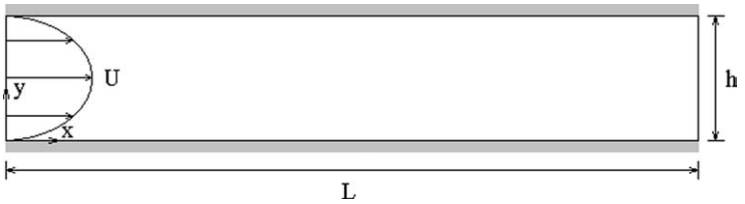

Fig. 1. Poiseuille flow in a planar channel.

where $G_N(t)$ is defined as

$$G_N(t) = \cosh\left(\frac{\beta_N t}{2S_1}\right) + \left[\frac{1 + N^2(S_2 - 2S_1)}{\beta_N}\right]\sinh\left(\frac{\beta_N t}{2S_1}\right) \tag{23}$$

and the other factors are:

$$N = (2n-1)\pi, \tag{24}$$

$$S_1 = \frac{We}{Re}, \tag{25}$$

$$S_2 = \beta S_1, \tag{26}$$

$$\alpha_N = 1 + S_2 N^2, \tag{27}$$

$$\beta_N = ((1 + S_2 N^2)^2 - 4S_1 N^2)^{1/2}. \tag{28}$$

The stress components are given by

$$\tau_{xx}(y,t) = 2ReC_{xy}(S_1, y)\left[A'(y)\exp\left(-\frac{t}{S_1}\right) - 32\sum_{n=1}^{\infty}\frac{\cos(Ny)}{N^2}I_N(t)\right] \tag{29}$$

$$+ 2ReA'(y)(1-\beta)\left[S_1 A'(y) - 32\sum_{n=1}^{\infty}\frac{\cos(Ny)}{N^2}H_N(t)\right]$$

$$-\frac{64ReA'(y)(1-\beta)}{S_1}\sum_{m=1}^{\infty}\frac{\cos(My)}{M^2}J_M(t) + \frac{2048Re(1-\beta)}{S_1}$$

$$\times\sum_{n,m=1}^{\infty}\frac{\cos(Ny)}{N^2}\frac{\cos(My)}{M^2}K_{NM}(t) + C_{xx}(y)\exp\left(-\frac{t}{S_1}\right), \tag{30}$$

$$\tau_{xy}(y,t) = \frac{(1-\beta)}{S_1}\left[S_1 A'(y) - 32\sum_{n=1}^{\infty}\frac{\cos(Ny)}{N^2}H_N(t)\right], + C_{xy}(y)\exp\left(-\frac{t}{S_1}\right), \tag{31}$$

$$\tau_{yy}(y,t) = 0,$$

where $M = (2m-1)\pi$, the function $H_N(t)$ is related to $G_N(t)$ by

$$H_N(t) = \left(\frac{\beta}{N} - \frac{\alpha_N}{2S_1 N^3}\right)G_N(t) + \frac{1}{N^3}G'_N(t)$$

and C_{xy} and C_{xx} are time-independent functions defined by the requirement that τ_{xy} and τ_{xx} are zero at $t = 0$. Details of the other coefficients are given in [4].

The transient development of the stress can exhibit both overshoots and undershoots as it evolves toward the steady-state solution. The problem has a smooth solution, being a pure transient shear flow, with a shear boundary layer at the channel walls and no shear along the centerline. There are no geometric singularities in the flow. Here, interest lies solely in determining the quality of the numerical solutions, evolved over time, and in detecting sensitivity to numerical instability for the algorithms under consideration.

For $\beta = 1/9$, the analytical solution displays overshoots and undershoots in the streamwise velocity component and the stress components, as *We* is increased from a value of zero to unity. As *We* is increased beyond unity, the velocity overshoot increases, whilst the velocity undershoot and stress overshoot/undershoot are damped. Once *We* reaches 100 there is no velocity undershoot or stress overshoot/undershoot. Also of interest is the relative settling times taken for velocity and stress components to settle down to their steady-state values. For $We < 1$, velocity and stress components take approximately the same time to achieve such states. However, for $We \geqslant 1$, the normal stress components take longer to attain their steady-state values as compared with the velocity components and the shear stress. Reproducing these features is a severe test of the time accuracy of any transient algorithm, given the different time-scales involved.

4. Temporal discretization

The governing equations are discretized in time using three distinct temporal schemes. These schemes will be compared and contrasted with respect to stability for unsteady plane Poiseuille flow.

4.1. Euler/Euler

This temporal discretization is a first-order scheme, using an Euler scheme to approximate the material time derivatives in the momentum and constitutive equations, and also an Euler scheme for the deformation terms:

- The material derivative
  The Euler approximation of the material derivative of a function $\mathbf{G}$ is

$$\frac{\mathrm{D}\mathbf{G}}{\mathrm{D}t} = \frac{\partial \mathbf{G}}{\partial t} + \mathbf{u}\cdot\nabla\mathbf{G} \approx \frac{\mathbf{G}^{n+1} - \mathbf{G}^{n}}{\Delta t} + \mathbf{u}^{n}\cdot\nabla\mathbf{G}^{n}. \tag{32}$$

- The deformation terms
  An Euler approximation for the deformation terms, calculated explicitly at the old time level, is

$$\nabla\mathbf{u}\cdot\boldsymbol{\tau} + \boldsymbol{\tau}\cdot(\nabla\mathbf{u})^{\mathrm{T}} \approx \nabla\mathbf{u}^{n}\cdot\boldsymbol{\tau}^{n} + \boldsymbol{\tau}^{n}\cdot(\nabla\mathbf{u}^{n})^{\mathrm{T}}. \tag{33}$$

4.2. OIFS2/AB2

This scheme uses two second-order temporal discretizations. A second-order Operator Integration Factor Splitting (OIFS) technique for the material derivatives of the velocity and the stress, and a second-order Adams–Bashforth (AB) approximation for the deformation terms:

- The material derivative
  The discretization of the material derivatives of both the velocity in the momentum equations, and the stress in the constitutive equation, will be obtained using a second-order OIFS scheme (see [22]). The material derivative of a function $\mathbf{G}$ is approximated as

$$\frac{\mathrm{D}\mathbf{G}}{\mathrm{D}t} = \frac{\partial \mathbf{G}}{\partial t} + \mathbf{u}\cdot\nabla\mathbf{G} \approx \frac{1}{2\Delta t}\left(3\mathbf{G}^{n+1} - 4\tilde{\mathbf{G}}(t^{n+1}) + \tilde{\tilde{\mathbf{G}}}(t^{n+1})\right). \tag{34}$$

The approximations $\tilde{\mathbf{G}}(t^{n+1})$ and $\tilde{\tilde{\mathbf{G}}}(t^{n+1})$ are the solutions at time $t = t^{n+1}$ of the pure convection problems

$$\frac{\partial \tilde{\mathbf{G}}}{\partial t} = -\mathbf{u}^{*}\cdot\nabla\tilde{\mathbf{G}}, \quad t \in [t^{n}, t^{n+1}] \quad \text{with } \tilde{\mathbf{G}}(\mathbf{x}, t^{n}) = \mathbf{G}^{n}(\mathbf{x}), \tag{35}$$

and

$$\frac{\partial \tilde{\tilde{\mathbf{G}}}}{\partial t} = -\mathbf{u}^* \cdot \nabla \tilde{\tilde{\mathbf{G}}}, \quad t \in [t^{n-1}, t^{n+1}] \quad \text{with } \tilde{\tilde{\mathbf{G}}}(\mathbf{x}, t^{n-1}) = \mathbf{G}^{n-1}(\mathbf{x}), \tag{36}$$

where $\mathbf{u}^*$ is a second-order approximation for the velocity at intermediate time levels given by

$$\mathbf{u}^* = \frac{(t - t^{n-1})}{\Delta t}\mathbf{u}^n + \left(1 - \frac{(t - t^{n-1})}{\Delta t}\right)\mathbf{u}^{n-1}. \tag{37}$$

A fourth-order explicit Runge–Kutta (RK4) method is used to solve these initial value problems. In the RK4 method, an additional time step is required. This time step h is defined as $h = \Delta t/M$, with M the number of RK4 iterations per outer time step, and $\Delta t = t^{n+1} - t^n$.

- The deformation terms

An explicit second-order Adams–Bashforth (AB) scheme is used to approximate the deformation terms at the new time level $t = t^{n+1}$. The scheme is given by (see Karniadakis and Sherwin [15])

$$\mathbf{F}^{n+1} \approx \sum_{q=0}^{J-1} \beta_q \mathbf{F}^{n+1-q}. \tag{38}$$

The factor J is the order of the AB scheme. For the second-order approximation ($J = 2$), the coefficients β_q are given by

$$\beta_0 = 0, \quad \beta_1 = \tfrac{3}{2}, \quad \beta_2 = -\tfrac{1}{2}, \tag{39}$$

which yields the approximation

$$\mathbf{F}^{n+1} \approx \tfrac{3}{2}\mathbf{F}^n - \tfrac{1}{2}\mathbf{F}^{n-1}. \tag{40}$$

This is applied to the deformation terms, where

$$\mathbf{F} = (\nabla \mathbf{u} \cdot \boldsymbol{\tau} + \boldsymbol{\tau} \cdot (\nabla \mathbf{u})^{\mathrm{T}}). \tag{41}$$

4.3. BDF2/EX2

This is another scheme that uses two second-order temporal discretizations. It comprises a second-order Backward Differentiation Formula (BDF) for the material derivatives of the velocity and the stress, and a second-order Extrapolation Scheme (EX) for the deformation terms:

- The material derivative

The second-order Backward Differentiation Formula, as used by Fiétier and Deville [8], approximates the material derivative of a function $\mathbf{G}$ as

$$\frac{\mathrm{D}\mathbf{G}}{\mathrm{D}t} = \frac{\partial \mathbf{G}}{\partial t} + \mathbf{u} \cdot \nabla \mathbf{G} \approx \frac{3\mathbf{G}^{n+1} - 4\mathbf{G}^n + \mathbf{G}^{n-1}}{2\Delta t} + 2\mathbf{u}^n \cdot \nabla \mathbf{G}^n - \mathbf{u}^{n-1} \cdot \nabla \mathbf{G}^{n-1}. \tag{42}$$

- The deformation terms

The second-order Extrapolation Scheme, as used by Fiétier and Deville [8], approximates the deformation terms as

$$\mathbf{F}^{n+1} \approx 2\mathbf{F}^n - \mathbf{F}^{n-1}. \tag{43}$$

4.4. The semi-discrete equations

Substituting the temporal discretizations for the material derivative and the deformation terms into the equations at the new time level t^{n+1}, gives the semi-discrete equations. The general form of these equations is:

$$\begin{aligned} &\nabla \cdot \mathbf{u}^{n+1} = 0, \\ &M_1 \boldsymbol{u}^{n+1} + \nabla p^{n+1} - \nabla \cdot \boldsymbol{\tau}^{n+1} - \beta \nabla^2 \mathbf{u}^{n+1} = \mathbf{f}^n(\mathbf{u}, \boldsymbol{\tau}), \\ &C_1 \boldsymbol{\tau}^{n+1} - 2(1-\beta)\mathbf{d}^{n+1} = \mathbf{H}^n(\mathbf{u}, \boldsymbol{\tau}). \end{aligned} \tag{44}$$

The parameter M_1 and the vector $\mathbf{f}^n(\mathbf{u}, \boldsymbol{\tau})$ are defined in Table 1 for the three temporal schemes. Similarly, the parameter C_1 and the tensor $\mathbf{H}^n(\mathbf{u}, \boldsymbol{\tau})$ are defined in Table 2.

5. Spectral element discretization

The spectral element method (see Maday and Patera [21], for example) is applied to the weak formulation of the semi-discrete equations (44). These equations constitute a generalized three-field Stokes problem. Suitable function spaces are chosen for the dependent variables. The velocity is chosen to be in a subspace, $\mathscr{V}$, of $[H^1(\Omega)]^2$ whose elements satisfy the prescribed velocity boundary conditions. The appropriate spaces for pressure and stress are:

$$\mathscr{P} = [L^2(\Omega)],$$

$$\mathscr{T} = [L^2(\Omega)]_s^4.$$

For this choice of function spaces, Gerritsma and Phillips [12] have shown that the integrals in the weak formulation are well-defined for the Stokes problem. This choice of function spaces is not appropriate, of course, for the weak formulation of the full problem. The resulting weak formulation of (44) is then: Find $(\mathbf{u}^{n+1}, p^{n+1}, \boldsymbol{\tau}^{n+1}) \in \mathscr{V} \times \mathscr{P} \times \mathscr{T}$, such that:

Table 1
The parameter M_1 and the vector $\mathbf{f}^n(\mathbf{u}, \boldsymbol{\tau})$ for the three temporal schemes

Scheme	M_1	$\mathbf{f}^n(\mathbf{u}, \boldsymbol{\tau})$
Euler/Euler	$\frac{Re}{\Delta t}$	$Re(\frac{\mathbf{u}^n}{\Delta t} - \mathbf{u}^n \cdot \nabla \mathbf{u}^n)$
OIFS2/AB2	$\frac{3Re}{2\Delta t}$	$\frac{Re}{2\Delta t}(4\tilde{\boldsymbol{u}}(t^{n+1}) - \tilde{\tilde{\boldsymbol{u}}}(t^{n+1}))$
BDF2/EX2	$\frac{3Re}{2\Delta t}$	$\frac{Re}{2\Delta t}(4\boldsymbol{u}^n - \boldsymbol{u}^{n-1}) - Re(2\mathbf{u}^n \cdot \nabla \mathbf{u}^n - \mathbf{u}^{n-1} \cdot \nabla \mathbf{u}^{n-1})$

Table 2
The factor C_1 and the tensor $\mathbf{H}^n(\mathbf{u}, \boldsymbol{\tau})$ for the three temporal schemes

Scheme	C_1	$\mathbf{H}^n(\mathbf{u}, \boldsymbol{\tau})$
Euler/Euler	$1 + \frac{We}{\Delta t}$	$We(\frac{\boldsymbol{\tau}^n}{\Delta t} - \mathbf{u}^n \cdot \nabla \boldsymbol{\tau}^n + \mathbf{F}^n)$
OIFS2/AB2	$1 + \frac{3We}{2\Delta t}$	$\frac{We}{2\Delta t}(4\tilde{\boldsymbol{\tau}}(t^{n+1}) - \tilde{\tilde{\boldsymbol{\tau}}}(t^{n+1})) + \frac{We}{2}(3\mathbf{F}^n - \mathbf{F}^{n-1})$
BDF2/EX2	$1 + \frac{3We}{2\Delta t}$	$\frac{We}{2\Delta t}(4\boldsymbol{\tau}^n - \boldsymbol{\tau}^{n-1}) + We(2\mathbf{F}^n - \mathbf{F}^{n-1})$ $-We(2\mathbf{u}^n \cdot \nabla \boldsymbol{\tau}^n - \mathbf{u}^{n-1} \cdot \nabla \boldsymbol{\tau}^{n-1})$

The function $\mathbf{F}$ represents the deformation terms: $\mathbf{F} = (\nabla \mathbf{u} \cdot \boldsymbol{\tau} + \boldsymbol{\tau} \cdot (\nabla \mathbf{u})^{\mathrm{T}})$.

$$
\begin{aligned}
&d(\mathbf{u}^{n+1}, q) = 0 \quad \forall q \in \mathscr{P}, \\
&M_1 c(\mathbf{u}^{n+1}, \mathbf{v}) + \beta e(\mathbf{u}^{n+1}, \mathbf{v}) - d^*(p^{n+1}, \mathbf{v}) + b(\boldsymbol{\tau}^{n+1}, \mathbf{v}) = (\mathbf{f}^n, \mathbf{v}) \quad \forall \mathbf{v} \in \mathscr{V}, \\
&C_1 a(\boldsymbol{\tau}^{n+1}, \boldsymbol{\sigma}) - (1-\beta) b^*(\mathbf{u}^{n+1}, \boldsymbol{\sigma}) = (\mathbf{H}^n, \boldsymbol{\sigma}) \quad \forall \boldsymbol{\sigma} \in \mathscr{T},
\end{aligned} \tag{45}
$$

where the bilinear forms $a(\cdot,\cdot)$, etc., are defined by:

$$a(\boldsymbol{\tau}, \boldsymbol{\sigma}) = \int_\Omega \boldsymbol{\tau} : \boldsymbol{\sigma} \, \mathrm{d}\Omega,$$

$$b(\boldsymbol{\tau}, \mathbf{v}) = -\int_\Omega \nabla \cdot \boldsymbol{\tau} : \mathbf{v} \, \mathrm{d}\Omega = \int_\Omega \boldsymbol{\tau} : \nabla \mathbf{v} \, \mathrm{d}\Omega,$$

$$b^*(\mathbf{u}, \boldsymbol{\sigma}) = \int_\Omega \nabla \mathbf{u} : \boldsymbol{\sigma} \, \mathrm{d}\Omega,$$

$$c(\mathbf{u}, \mathbf{v}) = \int_\Omega \mathbf{u} \cdot \mathbf{v} \, \mathrm{d}\Omega,$$

$$d(\mathbf{u}, q) = \int_\Omega \nabla \cdot \mathbf{u} q \, \mathrm{d}\Omega,$$

$$d^*(p, \mathbf{v}) = -\int_\Omega \nabla p \mathbf{v} \, \mathrm{d}\Omega = \int_\Omega p \nabla \cdot \mathbf{v} \, \mathrm{d}\Omega,$$

$$e(\mathbf{u}, \mathbf{v}) = -\int_\Omega \nabla^2 \mathbf{u} : \mathbf{v} \, \mathrm{d}\Omega = \int_\Omega \nabla \mathbf{u} : \nabla \mathbf{v} \, \mathrm{d}\Omega.$$

The bilinear forms $a(\cdot,\cdot)$, $b(\cdot,\cdot)$, $c(\cdot,\cdot)$, $d(\cdot,\cdot)$ and $e(\cdot,\cdot)$ induce continuous linear operators $A : \mathscr{T} \to \mathscr{T}'$, $B : \mathscr{T} \to \mathscr{V}'$, $C : \mathscr{V} \to \mathscr{V}'$, $D : \mathscr{T} \to \mathscr{P}'$ and $E : \mathscr{V} \to \mathscr{V}'$, such that:

$$[A\boldsymbol{\tau}, \boldsymbol{\sigma}] = a(\boldsymbol{\tau}, \boldsymbol{\sigma}) \quad \forall \boldsymbol{\tau}, \boldsymbol{\sigma} \in \mathscr{T},$$

$$[B\boldsymbol{\tau}, \mathbf{v}] = b(\boldsymbol{\tau}, \mathbf{v}) \quad \forall \boldsymbol{\tau} \in \mathscr{T} \quad \forall \mathbf{v} \in \mathscr{V},$$

$$[B^*\mathbf{u}, \boldsymbol{\sigma}] = b^*(\mathbf{u}, \boldsymbol{\sigma}) \quad \forall \mathbf{u} \in \mathscr{V} \quad \forall \boldsymbol{\sigma} \in \mathscr{T},$$

$$[C\mathbf{u}, \mathbf{v}] = c(\mathbf{u}, \mathbf{v}) \quad \forall \mathbf{u}, \mathbf{v} \in \mathscr{V},$$

$$[D\mathbf{u}, q] = d(\mathbf{u}, q) \quad \forall \mathbf{u} \in \mathscr{V} \quad \forall q \in \mathscr{P},$$

$$[D^*p, \mathbf{v}] = d^*(p, \mathbf{v}) \quad \forall p \in \mathscr{P} \quad \forall \mathbf{v} \in \mathscr{V},$$

$$[E\mathbf{u}, \mathbf{v}] = e(\mathbf{u}, \mathbf{v}) \quad \forall \mathbf{u}, \mathbf{v} \in \mathscr{V}.$$

In this notation, the dual problem to (45) is:

$$D\mathbf{u}^{n+1} = 0, \quad \text{in } \mathscr{P}',$$

$$(M_1C + \beta E)\mathbf{u}^{n+1} - D^* p^{n+1} + B\boldsymbol{\tau}^{n+1} = \mathbf{f}, \quad \text{in } \mathscr{V}', \tag{46}$$

$$C_1 A\boldsymbol{\tau}^{n+1} - (1-\beta)B^*\mathbf{u}^{n+1} = \mathbf{H}, \quad \text{in } \mathscr{T}'.$$

In the spectral element method, finite dimensional approximations to these operators are constructed. The spatial discretization of the physical domain Ω of the planar channel, involves dividing Ω into K non-overlapping spectral elements Ω_k, $1 \leqslant k \leqslant K$, such that $\cup_{k=1}^{K}\Omega_k = \Omega$. We denote by $\mathbb{P}_N(\Omega_k)$ the space of all polynomials on Ω_k of degree less than or equal to N, and further define $P_N(\Omega) = \{\phi : \phi|_{\Omega_k} \in \mathbb{P}_N(\Omega_k)\}$. Each of the spectral elements is mapped onto a parent element $D = [-1,1] \times [-1,1]$, where each point $(\xi,\eta) \in D$ is associated with a point $(x(\xi,\eta), y(\xi,\eta)) \in \Omega_k$. The dependent variables are approximated on D using Lagrangian interpolants of degree N in both spatial directions, based on the Gauss–Lobatto–Legendre points. This creates a Gauss–Lobatto–Legendre grid inside the spectral elements. Fig. 2 shows a spectral element mesh for a planar channel with $K = 8$ and approximating polynomials of degree $N = 4$ within each element.

The discrete approximation spaces must satisfy a compatibility condition to ensure that the problem is well-posed. For spectral elements Maday et al. [20] have shown that this LBB condition is satisfied when the velocity approximation space is the polynomial space $P_N(\Omega)$, and the pressure approximation space is $P_{N-2}(\Omega)$. A Gauss–Lobatto quadrature rule will be used to integrate the velocities, whereas a Gauss quadrature rule integrates the pressures. The stress will be approximated by polynomials in the space $P_N(\Omega)$ as well, with the difference that stresses are allowed to be discontinuous over element boundaries. Gerritsma and Phillips [11] have shown that this is a sufficient condition for stability of the corresponding three-field Stokes problem.

5.1. The discrete equations

Discretizing the weak formulation using spectral approximations, yields the following set of discrete equations:

$$D_N\mathbf{u}_N^{n+1} = 0,$$

$$(M_1C_N + \beta E_N)\mathbf{u}_N^{n+1} - D_N^{\mathrm{T}}\mathbf{p}_N^{n+1} + B_N\boldsymbol{\tau}_N^{n+1} = \mathbf{f}_N, \tag{47}$$

$$C_1A_N\boldsymbol{\tau}_N^{n+1} - (1-\beta)B_N^{\mathrm{T}}\mathbf{u}_N^{n+1} = \mathbf{H}_N,$$

where D_N and B_N are the discrete divergence operators acting on velocity and stress, respectively, D_N^{T} and B_N^{T} are gradient operators acting on pressure and velocity, E_N is the discrete Laplace operator, C_N and A_N are the discrete velocity and stress mass matrices, and $\mathbf{f}_N$ and $\mathbf{H}_N$ denote the discrete forms of the right-hand sides of (46). Combining the momentum equation and the constitutive equation yields

$$-D_N^{\mathrm{T}}\mathbf{p}_N^{n+1} + H_N\mathbf{u}_N^{n+1} = \mathbf{f}_N - \frac{1}{C_1}B_NA_N^{-1}\mathbf{H}_N. \tag{48}$$

Fig. 2. Spectral element mesh for a planar channel with $K = 8$ and $N = 4$.

In which H_N is the discrete Helmholtz-like operator, given by

$$H_N = \frac{(1-\beta)}{C_1} B_N A_N^{-1} B_N^{\mathrm{T}} + M_1 C_N + \beta E_N. \tag{49}$$

Eliminating the velocity using the discrete continuity equation, yields the equation that the pressure has to satisfy, i.e.

$$D_N H_N^{-1} D_N^{\mathrm{T}} \mathbf{p}_N^{n+1} = -D_N H_N^{-1} \left(\mathbf{f}_N - \frac{1}{C_1} B_N A_N^{-1} \mathbf{H}_N \right). \tag{50}$$

The operator $U_N = D_N H_N^{-1} D_N^{\mathrm{T}}$ is known as the Uzawa operator. Simplified, the pressure equation may be written as

$$U_N \mathbf{p}_N^{n+1} = \mathbf{b}_N, \tag{51}$$

where $\mathbf{b}_N$ is the right-hand side of (50).

5.2. Boundary conditions

No-slip and no-penetration conditions are applied on the walls $y = 0$ and $y = 1$. To obtain the solution of the steady problem using the time-dependent algorithm the steady parabolic velocity profile (17) is prescribed at inflow and outflow and the steady values of the stress components given by (18)–(20) are prescribed at inflow. Elsewhere in the domain zero initial conditions are used for velocity and stress.

For the transient start-up problem, time-dependent boundary conditions based on the analytical solution of Waters and King [33] given in Section 3 are applied at inflow. Elsewhere the initial conditions on velocity and stress are set to be zero.

Note that for both the steady and transient problems Dirichlet conditions on the stress at inflow are only prescribed when the Weissenberg number is nonzero.

5.3. Preconditioned iterative methods

To solve the pressure equation (51), a nested preconditioned conjugate gradient (PCG) method is used (see Deville et al. [5], for example). This requires the inversion of both the Uzawa operator $U = DH^{-1}D^{\mathrm{T}}$ and the Helmholtz operator H. The inversion of the Helmholtz operator is nested within the inversion of the Uzawa operator.

Since the Uzawa operator is only positive *semi*-definite, problems arise when trying to reach convergence in the PCG method when a tolerance of less than 10^{-14} is prescribed. The tolerance becomes harder to attain with increasing Weissenberg number. The indefiniteness of the Uzawa operator can be removed by adding the domain integral of the pressure to the right-hand side of the continuity equation. The Uzawa operator for the modified problem is then positive definite. This modification of the continuity equation ensures that the pressure approximation has a zero mean value.

The pressure mass matrix is used as a preconditioner for the Uzawa operator. The preconditioner used for the Helmholtz operator is based on an overlapping Schwarz method developed by Fischer [10] for spectral element discretizations.

The zero volume of pressure condition enforces the continuity constraint to be satisfied at all iterations within the PCG iteration. This is done by replacing the continuity equation by

$$\nabla \cdot \mathbf{u} = -\alpha \int_\Omega p \, \mathrm{d}\Omega, \tag{52}$$

where α is a positive constant. Integrating this equation over Ω and using Green's theorem, one can show that

$$\int_{\Omega} p \, \mathrm{d}\Omega = 0. \tag{53}$$

So this formulation will automatically ensure that $p \in L_0^2(\Omega)$, as well as leading to a better conditioned problem in the sense that the condition number of the discrete Uzawa operator is lower than that for the original formulation for a range of values of α. In evaluating the right-hand side of (47) the pressure is integrated over all elements Ω in the computational domain. After discretization of the integral, the modified discrete continuity equation is

$$D_N \mathbf{u}_N = -\alpha Q_N \mathbf{p}_N, \tag{54}$$

where Q_N is a matrix of rank one. This replaces the first equation in (47). The pressure equation (51) will now be of the form

$$(U_N + \alpha Q_N)\mathbf{p}_N = \mathbf{b}_N. \tag{55}$$

The efficiency of the algorithm has been tested for different values of α, for the channel flow problem described in Section 6.1.1. The only difference is that the convergence criterion for the outer PCG iteration to invert the Uzawa operator is set to 10^{-20} and the convergence criterion for the inner PCG iteration to invert the Helmholtz operator is set to 10^{-24}. Table 3 and Fig. 3 show that there is an optimum value of α, for the efficiency of the Uzawa inversion, although the algorithm behaves well for a wide range of values of α. The optimum value of α may vary when either the problem or the convergence criteria are changed. The value used for the remainder of this paper is $\alpha = 1$.

5.4. Preconditioners for the Uzawa operator

Three types of preconditioner have been tested for the Uzawa operator. These are:

- $P_{\mathrm{U}} = I$, the unit matrix, which means no preconditioner is used.
- $P_{\mathrm{U}} = M_{\mathrm{p}}$, the pressure mass matrix.
- $P_{\mathrm{U}}^{-1} = C_{\mathrm{P}}^{-1} = (\frac{(1-\beta)}{C_{\mathrm{l}}} + \beta)M_{\mathrm{p}}^{-1} + M_{\mathrm{l}}(DC^{-1}D^{\mathrm{T}})^{-1}$, a preconditioner based on work by Cahouet and Chabard [3], and extended to viscoelastic models by Escriva et al. [7].

The preconditioner that was developed by Cahouet and Chabard [3] is based on the operator identity

$$-\nabla \cdot (a\mathbf{I} - b\nabla^2)^{-1}\nabla = (b\mathbf{I} - a(\nabla^2)^{-1})^{-1}, \tag{56}$$

where $\nabla \cdot (\frac{Re}{\Delta t}\mathbf{I} - \nabla^2)^{-1}\nabla$ arises from the continuous Navier–Stokes equations. The preconditioner was constructed so that it matches the asymptotic behaviour of the Uzawa operator in the steady Stokes and high Reynolds number limits. The appropriate preconditioner is

$$P_{\mathrm{U}}^{-1} = M_{\mathrm{p}}^{-1} + \frac{Re}{\Delta t}(DC^{-1}D^{\mathrm{T}})^{-1}. \tag{57}$$

Table 3
Average number of iterations in the Uzawa inversion within one time-step for different values of α

α	10^{-6}	10^{-4}	10^{-3}	5×10^{-3}	10^{-2}	10^{-1}	10^{0}	10^{2}
It_{U}	132.64	119.68	115.54	114.07	114.43	117.79	129.21	147.89

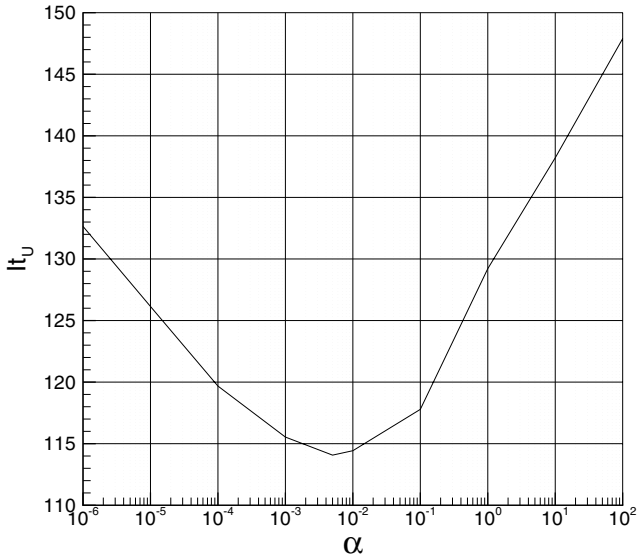

Fig. 3. Average number of iterations in the Uzawa inversion within one time-step as a function of α.

Escriva et al. [7] adopted this strategy for viscoelastic problems. Since the factors a and b in (56) were found to be

$$a = \frac{Re}{\Delta t} \quad \text{and} \quad b = \beta + \frac{1-\beta}{\frac{We}{\Delta t}+1}, \tag{58}$$

the following preconditioner was proposed:

$$P_{\mathrm{U}}^{-1} = \left(\beta + \frac{1-\beta}{\frac{We}{\Delta t}+1}\right) M_{\mathrm{p}}^{-1} + \frac{Re}{\Delta t}(DC^{-1}D^{\mathrm{T}})^{-1}. \tag{59}$$

This preconditioner may be effective in terms of reduction of numbers of iterations. However, to calculate the preconditioner itself, a further PCG iteration has to be used to invert the Laplacian, which in itself is very time consuming.

5.5. Preconditioners for the Helmholtz operator

The following two preconditioners have been tested for the inversion of the Helmholtz operator:

- $P_{\mathrm{H}} = I$, the unit matrix, which means no preconditioner is used.
- $P_{\mathrm{H}} = S_{\mathrm{P}}$, the overlapping Schwarz preconditioner, which is based on the classical additive Schwarz method developed by Dryja and Widlund [6].

The overlapping Schwarz preconditioner is based on solutions of similar local problems using finite element approximations on subdomains that overlap the spectral elements. In a problem with K spectral elements Ω_k, $k = 1, \ldots, K$, these subdomains $\tilde{\Omega}_k$ are the existing spectral elements extended by a constant number of Gauss–Lobatto–Legendre nodes in each direction into adjacent elements. Homogeneous Dirichlet conditions are assumed on the boundaries of these extended subdomains. Throughout this paper, the overlap will comprise two nodes. To provide the global coupling in the preconditioner, the solution on

one extra domain, known as the coarse grid, is needed. The coarse grid, also known as the skeleton spectral element grid, consists of the vertices of the spectral element mesh. The preconditioner may be written as

$$P_{\mathrm{H}}^{-1} = R_0^{\mathrm{T}} A_0^{-1} R_0 + \sum_{k=1}^{K} R_k^{\mathrm{T}} A_k^{-1} R_k, \tag{60}$$

where A_k is the stiffness matrix corresponding to the finite element approximation of the problem on the subdomain $\tilde{\Omega}_k$, and R_k and R_k^{T} are the restriction and interpolation operators, respectively, that map the spectral element space onto the finite element space and vice versa. The subscript 0 refers to the coarse grid problem.

6. Results

In this section the performance and efficiency of the preconditioners used to invert the Uzawa and Helmholtz operators are discussed. Next, a study of the steady Poiseuille flow is given, followed by results for the startup of plane Poiseuille flow. Finally, the effects on the numerical solution due to mesh refinement, the value of the parameter β, the timestep Δt, different temporal discretization schemes and the length of the channel are discussed.

6.1. Steady channel flow

To find steady solutions to the Poiseuille flow in a channel, two approaches are used in this paper. In this section, the fully developed flow is prescribed as a steady boundary condition. Starting with zero initial conditions, the solution will converge to the fully developed flow in the whole channel, using a transient algorithm. The transient development from the initial conditions is in this case only a means of finding the steady-state solution, and the time dependent start-up of the flow itself has no physical interpretation. In Section 6.2, the Waters and King solution will be used as a transient boundary condition. This time dependent solution may be physically interpreted as the start-up of Poiseuille flow of an Oldroyd B fluid.

For the steady channel flow, a parabolic profile is used to prescribe the steady velocity boundary condition at both inflow and outflow. The corresponding extra stress profiles are prescribed as boundary conditions only at the inflow of the channel. A no-slip condition is applied at the walls of the channel $y = 0$, and $y = h$. Zero initial conditions for both velocity and stress are assumed inside the domain.

6.1.1. Performance and efficiency of preconditioners

We begin our study of steady channel flow by investigating the performance of the different preconditioners described in Sections 5.4 and 5.5, for different values of N, K, Re and We for a channel with $L = 32$ and $h = 1$. The boundary conditions are based on the parabolic velocity profile $u = -6y(y-1)$.

The Euler/Euler temporal scheme is used, with a timestep $\Delta t = 0.1$. The convergence criteria for the PCG algorithms for the Uzawa and the Helmholtz operators are set to be 10^{-12} and 10^{-16}, respectively. The solution is assumed to be converged when the L^2-norm of the difference between two successive velocity and stress approximations is less than 10^{-6}. These L^2-norms are defined by:

$$||\Delta \mathbf{u}||_{L^2} = \left[\int_{\Omega} |u^{n+1} - u^n|^2 + |v^{n+1} - v^n|^2 \, \mathrm{d}\Omega \right]^{1/2}, \tag{61}$$

$$||\Delta\boldsymbol{\tau}||_{L^2} = \left[\int_{\Omega} |\tau_{xx}^{n+1} - \tau_{xx}^{n}|^2 + |\tau_{yy}^{n+1} - \tau_{yy}^{n}|^2 + 2|\tau_{xy}^{n+1} - \tau_{xy}^{n}|^2 \, \mathrm{d}\Omega \right]^{1/2}. \tag{62}$$

Summarizing, the parameters that have been used to test the performance of the preconditioners are (unless otherwise stated): $N = 8$, $K = 4$, $Re = 1$, $We = 0.1$, $\beta = 1/9$, $\Delta t = 0.1$, $L = 32$, $h = 1$. The distribution of the four equally sized elements is as is depicted in Fig. 6.

In Tables 4–7 the efficiency of the various preconditioners is indicated using three quantities. These are:

- The average number of iterations per time step, It_{U}, needed to invert the Uzawa operator.
- The average number of iterations, It_{H}, needed to invert the Helmholtz operator, averaged over the total number of Helmholtz inversions. Since the Helmholtz operator needs to be inverted in every Uzawa iteration, the total number of Helmholtz inversions equals the number of time steps times the average number of Uzawa iterations per time step, It_{U}.
- The average time to invert the Uzawa operator is given by Δt_{U}, in seconds. The computations are run on a Compaq XP1000 workstation.

The efficiency of the Cahouet–Chabard based preconditioner C_{P} for the Uzawa operator, is clear in terms of reduction of the number of iterations in the Uzawa PCG iteration. However, the calculation of this preconditioner, involves the inversion of the pseudo-Laplacian $(DC^{-1}D^{\mathrm{T}})^{-1}$. The number of iterations needed for this PCG inversion increases dramatically with increasing polynomial order, N, and number of elements, K. This reduces the performance of this preconditioner considerably. A solution might be to invert the Laplacian in pressure space E_{p}, which is cheaper, but may decrease the performance of the preconditioner in terms of iterations for the Uzawa iteration. In order to calculate E_{p}, derivatives of the test functions in pressure space are needed. This is beyond the scope of this paper.

Because of the poor performance of the Cahouet–Chabard preconditioner, the second choice of preconditioner for the Uzawa operator, the pressure mass matrix M_{p}^{*} will be used throughout the remainder of this paper. This preconditioner still gives a considerable reduction in the number of Uzawa iterations, and it is efficient since it only involves the inversion of a diagonal matrix.

The advantage of the overlapping Schwarz preconditioner for the Helmholtz operator is obvious. In all cases it provides reductions in both the number of iterations in the Helmholtz PCG loop and the time to

Table 4
Performance of the preconditioners with increasing polynomial order N

N	It_{U}	It_{H}	Δt_{U}	P_{U}	P_{H}
4	23.29	21.50	0.411	C_{P}	S_{P}
4	31.39	21.18	0.211	M_{p}^{*}	S_{P}
4	37.32	22.01	0.258	I	S_{P}
4	31.39	31.00	0.111	M_{p}^{*}	I
4	37.43	32.40	0.139	I	I
8	49.96	36.13	≈80	C_{P}	S_{P}
8	76.89	35.25	2.646	M_{p}^{*}	S_{P}
8	138.50	36.30	4.874	I	S_{P}
8	75.57	141.26	4.016	M_{p}^{*}	I
8	137.71	145.16	7.384	I	I
12	70.61	47.52	≈1800	C_{P}	S_{P}
12	103.18	48.64	13.37	M_{p}^{*}	S_{P}
12	231.04	44.95	25.599	I	S_{P}
12	103.54	308.41	29.954	M_{p}^{*}	I
12	231.64	284.51	62.513	I	I

To achieve a converged solution, 28 time steps were needed.

Table 5
Performance of the preconditioners with increasing number of elements K

K	It_U	It_H	Δt_U	P_U	P_H
4	49.96	36.13	≈80	C_P	S_P
4	76.89	35.25	2.646	M_p^*	S_P
4	138.50	36.30	4.874	I	S_P
4	75.57	141.26	4.016	M_p^*	I
4	137.71	145.16	7.384	I	I
8	73.96	41.54	≈320	C_P	S_P
8	109.71	41.60	8.016	M_p^*	S_P
8	189.18	38.77	13.080	I	S_P
8	106.32	165.35	12.896	M_p^*	I
8	188.39	152.97	21.336	I	I

The 4 elements are ordered as in Fig. 6, the 8 elements are ordered as in Fig. 2. A converged solution was obtained in 28 time steps.

Table 6
Performance of the preconditioners with different Reynolds number Re

Re	It_U	It_H	Δt_U	P_U	P_H
1	49.96	36.13	≈80	C_P	S_P
1	76.89	35.25	2.646	M_p^*	S_P
1	138.50	36.30	4.874	I	S_P
1	75.57	141.26	4.016	M_p^*	I
1	137.71	145.16	7.384	I	I
10	69.00	26.55	≈110	C_P	S_P
10	155.31	26.07	4.271	M_p^*	S_P
10	230.54	26.30	6.295	I	S_P
10	153.04	80.37	5.016	M_p^*	I
10	229.92	80.55	7.533	I	I

Converged solutions were obtained in 28 and 26 time steps for $Re = 1$ and $Re = 10$, respectively.

Table 7
Performance of the preconditioners with different Weissenber number We

We	It_U	It_H	Δt_U	P_U	P_H
0	46.57	39.46	≈75	C_P	S_P
0	64.14	38.97	2.376	M_p^*	S_P
0	129.43	39.02	4.747	I	S_P
0	65.00	153.44	3.626	M_p^*	I
0	130.29	155.02	7.262	I	I
0.1	49.96	36.13	≈80	C_P	S_P
0.1	76.89	35.25	2.646	M_p^*	S_P
0.1	138.50	36.30	4.874	I	S_P
0.1	75.57	141.26	4.016	M_p^*	I
0.1	137.71	145.16	7.384	I	I

The parameter β is set to zero. 28 time steps were needed to achieve a converged solution for $We = 0.1$, 7 time steps when $We = 0$.

reach convergence. Changes in the parameter β, the timestep Δt, the temporal discretization scheme and the length of the channel may have a considerable effect on the maximum attainable Weissenberg number. The results are discussed below.

6.1.2. Time integration method of material derivative/deformation terms

For the Oldroyd B and UCM models different time integration methods have been tested. The following parameters are used: $N = 4$, $K = 1$, $Re = 0$ and $Re = 0.1$, with a timestep $\Delta t = 0.1$. The channel length is $L = 64$, and height $h = 1$. The boundary conditions are based on the velocity profile $u = -4y(y-1),\ y \in [0,1]$.

The convergence criteria $||\Delta \mathbf{u}||_{L^2}$ and $||\Delta \boldsymbol{\tau}||_{L^2}$ norms are set to 10^{-8}. When these criterion are met, the Weissenberg number is increased, according to:

$$We = We + 0.05 \quad \text{if } We \leqslant 1, \tag{63}$$

$$We = We * \ 1.1 \quad \text{if } We > 1. \tag{64}$$

The convergence criteria on the residuals of the preconditioned conjugate gradient loops for the inversion of the Uzawa and Helmholtz operators are set to 10^{-9} and 10^{-14}, respectively.

In Table 8, the maximum attainable Weissenberg numbers for the Euler/Euler method and for BDF2/EX2 and OIFS2/AB2 are presented for the UCM model and for an Oldroyd B model with $\beta = 1/9$. The results in this table show that a nonzero Reynolds number clearly has a stabilizing effect on the calculations for the UCM model and the Oldroyd B model.

The calculations performed for the UCM model show that a larger maximum Weissenberg number can be achieved when a first-order temporal scheme is used rather than a second-order scheme. We do not have an explanation for this for the steady problem at the moment. However, we speculate that it is related to the relative regularity of the solutions to the UCM and Oldroyd B problems as indeed it is for the corresponding inertial transient problems.

6.1.3. Parameter β

Using the Euler/Euler scheme to approximate the material derivative and deformation terms, the Oldroyd B model has been tested for $\beta = 0$ (UCM), $\beta = 1/9$ and $\beta = 0.9$. The convergence criteria for $||\Delta \mathbf{u}||_{L^2}$ and $||\Delta \boldsymbol{\tau}||_{L^2}$ are set to 10^{-8}, and for the inversion of the Helmholtz operator, a preconditioner based on an overlapping Schwarz method has been used, with an overlap of two nodes. The mesh is defined by $N = 4$ and $K = 8$, ordered as in Fig. 2. The timestep is $\Delta t = 0.1$, the channel length is $L = 64$, and the height $h = 1$, with a parabolic inflow profile: $u = -4y(y-1),\ y \in [0,1]$. The convergence criteria are 10^{-9} for the Uzawa loop, and 10^{-14} for the Helmholtz loop.

In Table 9, the maximum attainable Weissenberg numbers for Reynolds numbers of $Re = 0$ and $Re = 1$ are given, with $\beta = 0$ (UCM) and $\beta = 1/9$ and $\beta = 0.9$. The influence of changes in the Reynolds number

Table 8
Maximum attainable Weissenberg numbers for different temporal discretizations and models, for a one element mesh with $N = 4$ and $L = 64$

	$We_{\max}$ ($Re = 0$)	$We_{\max}$ ($Re = 0.1$)
UCM		
Euler/Euler	8.95	17.45
OIFS2/AB2	6.73	8.95
BDF2/EX2	5.05	8.95
Oldroyd B		
Euler/Euler	28.10	34.00
OIFS2/AB2	28.10	34.00
BDF2/EX2	28.10	34.00

Table 9
Maximum attainable Weissenberg numbers for different values of β and Re, on a mesh with $K = 8$, $N = 4$ and $L = 64$

		$We_{\max}$
$Re = 0$	$\beta = 0$	1.77
	$\beta = 1/9$	1.77
$Re = 1$	$\beta = 0$	1.77
	$\beta = 1/9$	1.77
	$\beta = 0.9$	3.14

and the parameter β is less obvious than in the results for the one element case which are presented in Table 8. A high value of β however, clearly provides a more stable problem.

6.1.4. Timestep

For the Oldroyd B model with $\beta = 1/9$, $Re = 1$, and $We = 0.5$, different values for the timestep are tested. The other parameters are the same as in Section 6.1.3. Convergence for the norms of the stresses are shown in Fig. 4, for $\Delta t = 10^{-1}$ and $\Delta t = 10^{-3}$. Whereas the convergence of the stress approximation using the larger time step is predominantly monotonic until machine precision is reached, the convergence history for the smaller time step is more irregular and is undulatory in behaviour.

6.1.5. Number of elements and order of polynomial approximation

For the UCM ($\beta = 0$) model under the creeping flow assumption ($Re = 0$), different values for the number of elements K and the polynomial order N are tested. All other values are the same as in Section 6.1.3. For one element no Schwarz overlap based preconditioner is possible, so for the Helmholtz operator for one element, the identity is used (no preconditioner) in the PCG iteration.

Maximum attainable Weissenberg numbers are given in Table 10, for $K = 1$ with both $N = 4$ and $N = 8$, and $K = 8$ (as in Fig. 2), also with both $N = 4$ and $N = 8$. The ability of the model to produce valid results at high Weissenberg numbers decreases with increasing the mesh resolution.

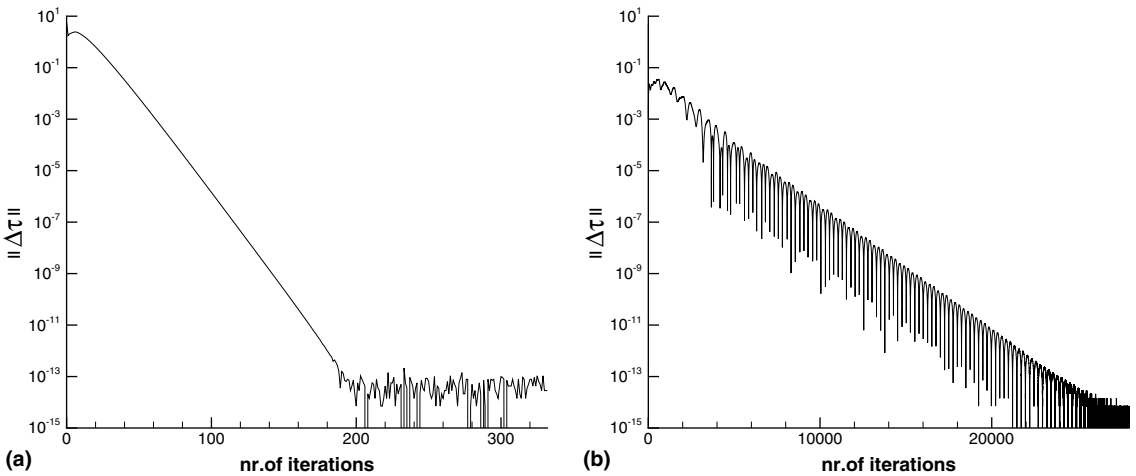

Fig. 4. Convergence of norms of stresses for (a) $\Delta t = 10^{-1}$ and (b) $\Delta t = 10^{-3}$, for an Oldroyd B model with $\beta = 1/9$, $Re = 1$, and $We = 0.5$, on a mesh with $K = 8$, $N = 4$ and $L = 64$.

Table 10
Maximum attainable Weissenberg numbers for different polynomial orders and number of elements, for a UCM model with $Re = 0$

		We_{max}
$N = 4$	$K = 1$	7.59
	$K = 8$	1.77
$N = 8$	$K = 1$	3.80
	$K = 8$	0.50

Fig. 5 shows a plot of $||\Delta\tau||_{L^2}$, against the non-dimensional time, for the mesh with $N = 8$ and $K = 8$. Only the last three Weissenberg numbers are plotted. The maximum attainable Weissenberg number is $We = 0.50$, and any higher value causes the solution to diverge.

6.1.6. Channel length

For an Oldroyd B model with $\beta = 1/9$, with a Reynolds number of $Re = 1$, different values for the length of the channel are tested. All other values are the same as before in the list in Section 6.1.3.

Maximum attainable Weissenberg numbers are given in Table 11. When the length of the channel is shortened, this maximum Weissenberg number decreases, notably in an almost linear fashion. This may represent the same behaviour of decreasing We_{max} with increasing mesh resolution, since a shorter channel is effectively a refinement of the mesh in the lengthwise direction.

6.2. Transient channel flow

Solutions to the planar start-up of channel flow of the Oldroyd B model, are calculated using the Waters and King solution for the start-up of Poiseuille flow as transient boundary conditions. The velocity solution is used at inflow and outflow, the stress solution only at inflow. All other initial conditions are zero.

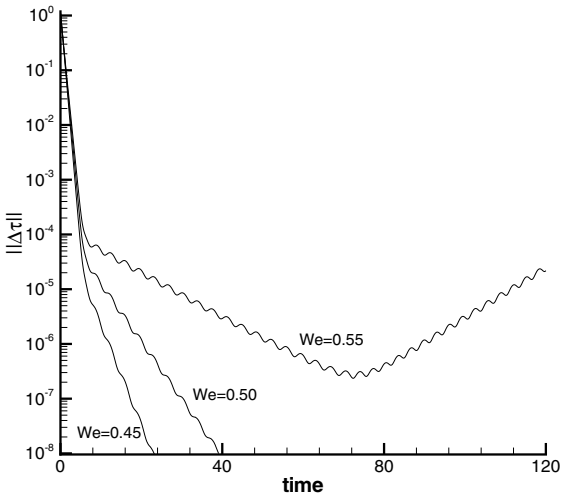

Fig. 5. Convergence plot of $||\Delta\tau||_{L^2}$, for a UCM model with $Re = 0$, on a mesh with $K = 8$, $N = 8$ and $L = 64$. Only the plots for the highest three Weissenberg numbers are shown.

Table 11
Maximum attainable Weissenberg for different channel lengths on a mesh with $K = 8$, $N = 4$, and $L = 64$, for an Oldroyd B model with $\beta = 1/9$, $Re = 1$

Channel length	We_{max}
8	0.25
16	0.45
32	0.90
64	1.77

The performance of the algorithm is shown by solving the transient start-up problem for an Oldroyd B model with $\beta = 1/9$. The Weissenberg and Reynolds numbers are fixed at $We = 1$ and $Re = 1$, the timestep is 10^{-2}, and $h = 1$. Convergence of the solution to the exact Waters and King solution is shown in Tables 12–15, for different values of N, L, K_x and K_y. Here K_x and K_y denote the number of spectral elements in the lengthwise and cross channel directions, respectively.

Table 12
Convergence behaviour for varying values of K_x and L, at a fixed value of $N = 6$

$K_x \times K_y$	N	$L = 8$	$L = 16$	$L = 32$	$L = 64$
1×2	6	C	C	C	C
2×2	6	4.10	10.80	C	C
3×2	6	2.10	5.30	22.00	C
4×2	6	1.00	3.50	11.20	C

A converged solution is denoted with a C. If the solution does not converge, the approximate time at which the solution diverges is given.

Table 13
Convergence behaviour for varying values of K_x and L, at a fixed value of $N = 4$

$K_x \times K_y$	N	$L = 8$	$L = 16$	$L = 32$	$L = 64$
2×2	4	12.10	C	C	C
4×2	4	3.00	12.60	C	C
6×2	4	1.30	5.60	C	C
8×2	4	0.90	3.00	13.00	C

A converged solution is denoted with a C. If the solution does not converge, the approximate time at which the solution diverges is given.

Table 14
Convergence behaviour for varying values of K_y and L, at a fixed value of $N = 6$

$K_x \times K_y$	N	$L = 8$	$L = 16$	$L = 32$
2×1	6	5.90	20.20	C
2×2	6	4.10	10.80	C
2×3	6	3.90	10.90	C
2×4	6	3.90	11.00	C

A converged solution is denoted with a C. If the solution does not converge, the approximate time at which the solution diverges is given.

Table 15
Convergence behaviour for varying values of K_y and L, at a fixed value of $N = 4$

$K_x \times K_y$	N	$L = 8$	$L = 16$
2×1	4	24.00	C
2×2	4	12.10	C
2×3	4	11.00	C
2×4	4	11.00	C

A converged solution is denoted with a C. If the solution does not converge, the approximate time at which the solution diverges is given.

From Table 12 it can be concluded that at a fixed channel length, increasing K_x results in poorer convergence behaviour. This is also the case if K_x is kept fixed, and the channel length is decreased. At a lower approximation order N, Table 13 shows that convergence is reached easier at the same values for K_x and L. This reflects the findings for the steady channel flow where either a decrease in channel length or an increase in the value of K_x or N resulted in lower maximum attainable Weissenberg numbers.

The influence of the number of elements in the cross channel direction, K_y, on the convergence behaviour is considerably weaker, as can be seen in Tables 14 and 15. Although divergence sets in slightly later when $K_y = 1$ only, no examples have been found where the choice of K_y influenced whether or not the solution eventually diverged. The results in Table 15, at a lower approximation order N, again show better convergence behaviour than the results at higher N in Table 14.

The exact solution that is prescribed at inflow, according to the Waters and King solution, is compared to the solution that is calculated at the Gauss–Lobatto point on the penultimate vertical gridline, i.e., one before the outflow of the channel. Fig. 6 shows the nodes A and B where the velocity is monitored, and the nodes C and D where the stresses are monitored.

The time-dependent solutions at these two points are superimposed in Fig. 7, where $K_y = 2$, $K_x = 4$, $L = 64$ and $N = 6$. Slight differences in the peak of the time-dependent solution can be observed. The spectral approximation of τ_{xx} overshoots the first peak in the exact solution by $\approx 2\%$. The spectral approximation of u, undershoots the first peak in the exact solution by less than 1%. No such under- or overshoots are observed in the comparison of the numerical and exact values for τ_{xy}. Apart from these differences, the curves are hardly distinguishable.

The length of the channel is now halved to $L = 32$, keeping K_y, K_x and N fixed. As can be seen in Table 12, the solution to this problem diverges at around $t = 11.20$. Fig. 8 shows this typical divergence behaviour of the numerical solution away from the exact solution. Although the transient numerical solution seems to follow the exact solution and to settle down to the steady-state solution, dramatic divergence sets in after a certain number of iterations. With all other parameters fixed this happens when either the channel is shortened or K_x is increased or N is increased. All of these actions represent refinement of the mesh in the lengthwise direction. Decreasing the timestep might delay the divergence slightly, but does not change the overall result.

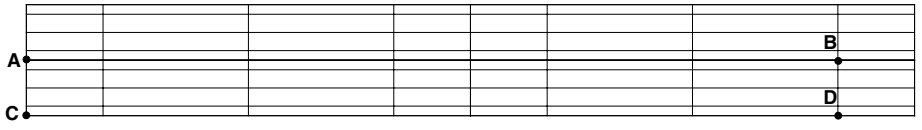

Fig. 6. The nodes where the velocity component u and the stress components τ_{xx} and τ_{xy} are monitored, on a mesh with $K_x = 2$, $K_y = 2$ and $N = 4$.

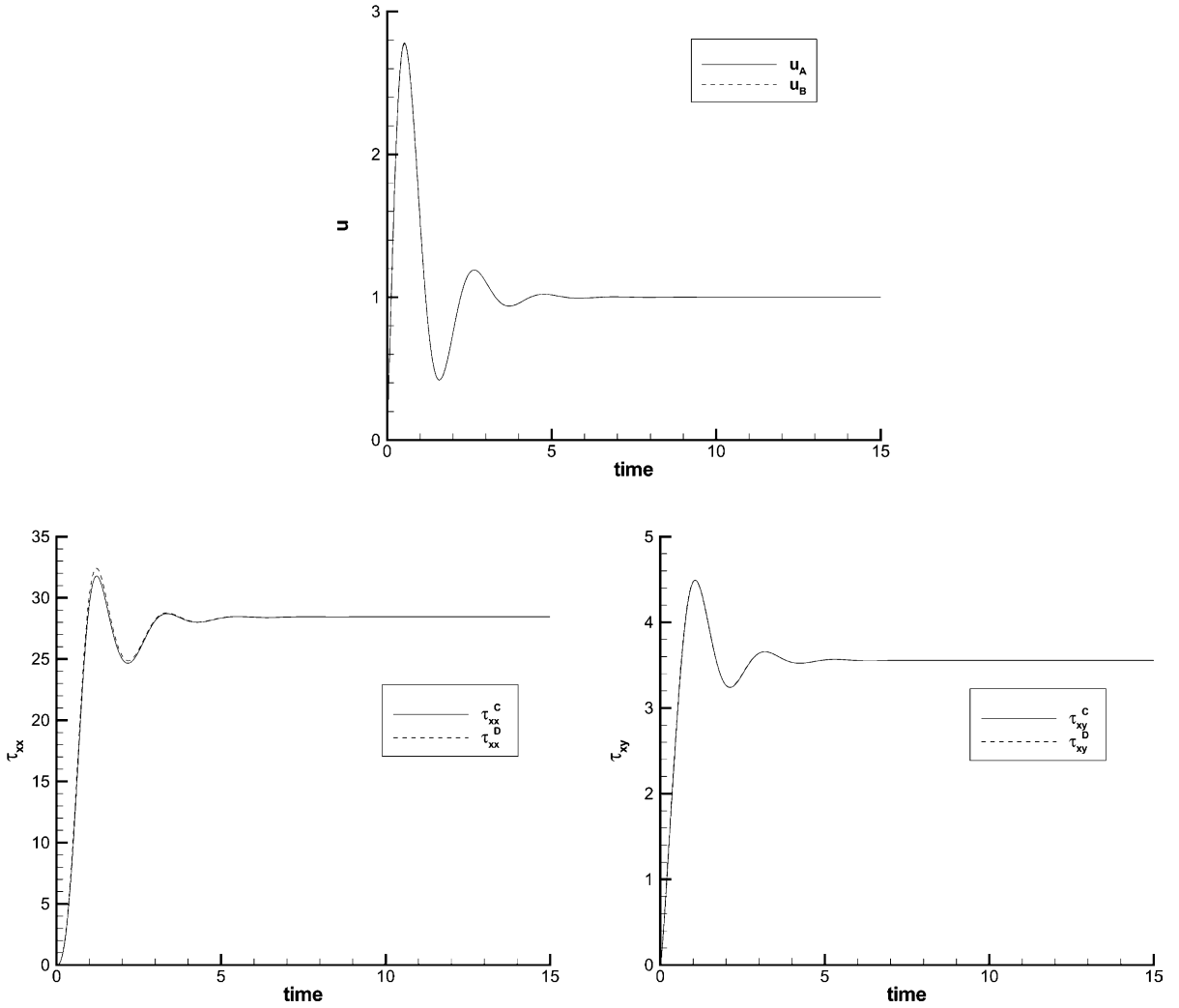

Fig. 7. Transient solution for a channel with $K = 8$ elements, with a distribution $K_x = 4$, $K_y = 2$ and $N = 6$, for $We = 1$ and $Re = 1$.

On meshes with $K_x = 1$, converged solutions can be found for higher Weissenberg numbers. This seems to suggest that the spatial discretization and, in particular, the presence of spectral element interfaces in the streamwise direction is partially responsible for the onset of spurious instabilities. Fiétier [9] showed that mesh discretization has a strong impact on the location of the eigenvalues of the associated generalized eigenvalue problem and therefore on numerical stability. This seems to be in agreement with statements made by Beris and Sureshkumar [32] and Wilson et al. [34] about the generation of spurious oscillations caused by the inadequate resolution of the continuous spectrum. Lozinski and Owens observed no limit on the critical Weissenberg number when solving this problem using a single spectral element. However, unlike the numerical simulations of Fiétier and Deville [8] and those under consideration in the present article, periodic boundary conditions were applied across the channel. Therefore, it is impossible to make a direct comparison with this work. However, we should comment that, in the

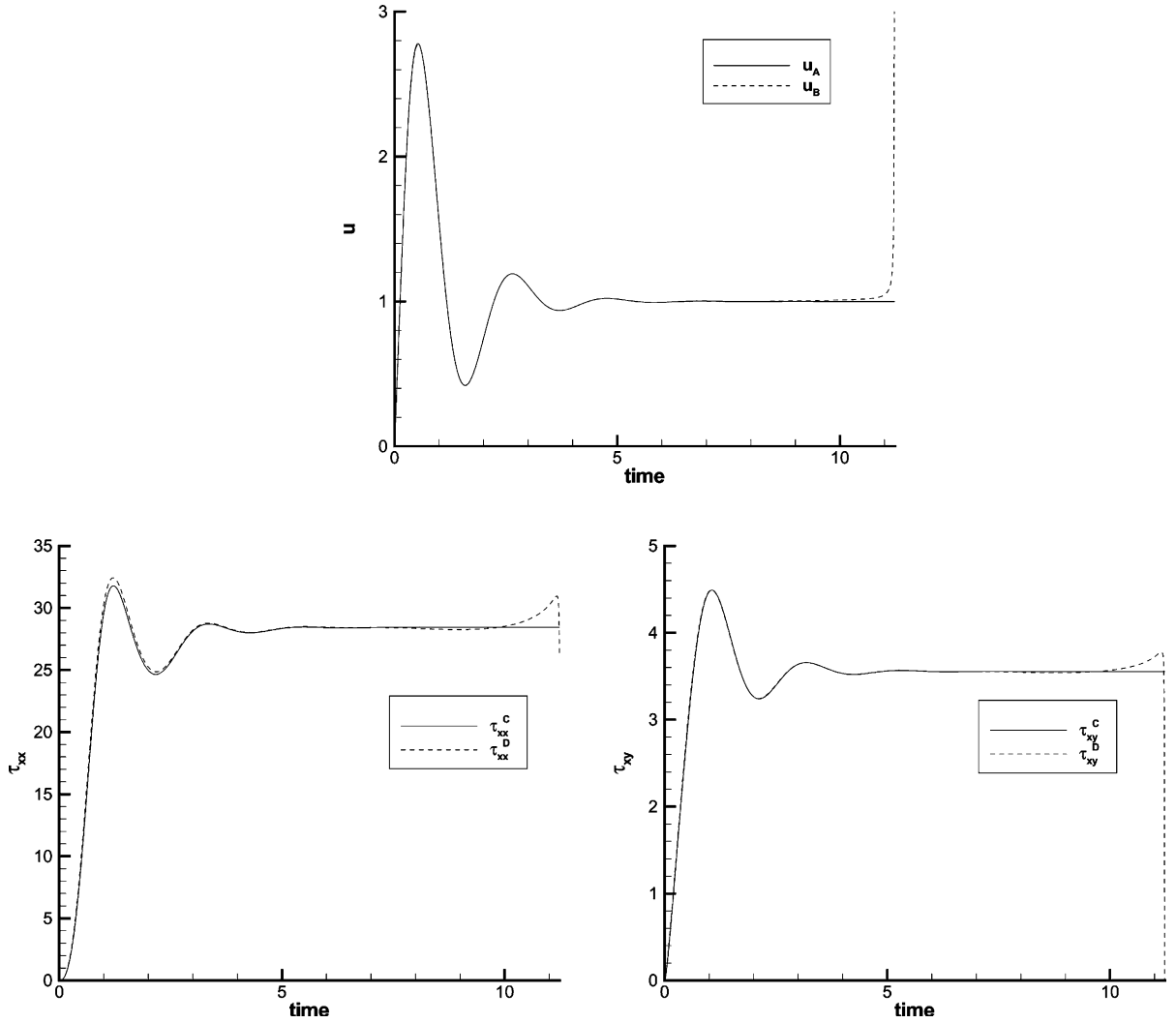

Fig. 8. Typical divergence of the numerical solution from the exact solution of a transient start-up of a channel flow. Divergence at around $t = 11.20$.

context of spectral methods, the imposition of periodic boundary conditions generally leads to the attainment of a higher critical value of the Weissenberg number compared with the imposition of Dirichlet conditions.

Converged solutions have been obtained for the Oldroyd B model ($\beta = 1/9$) for $We = 10$ and $We = 20$ with $Re = 1$ on a mesh with $K_x = 1$, $K_y = 1$, $L = 64$, $N = 4$ and $\Delta t = 10^{-2}$. Figs. 9 and 10 show the Waters and King solution at the points A and B, compared to the numerical solution at points B and D for $We = 10$ and $We = 20$, respectively. A very clear overshoot can be observed for τ_{xx}, but the profiles for u and τ_{xy} are hardly distinguishable. The normal stress τ_{xx} takes considerably longer (around a factor of 10 for $We = 20$) to reach its steady-state value compared with u and τ_{xy} and dominates the shear stress in absolute value. The same converged solutions have been found on meshes with $K_x = 1$, $K_y = 4$. Again, the value of K_y does not

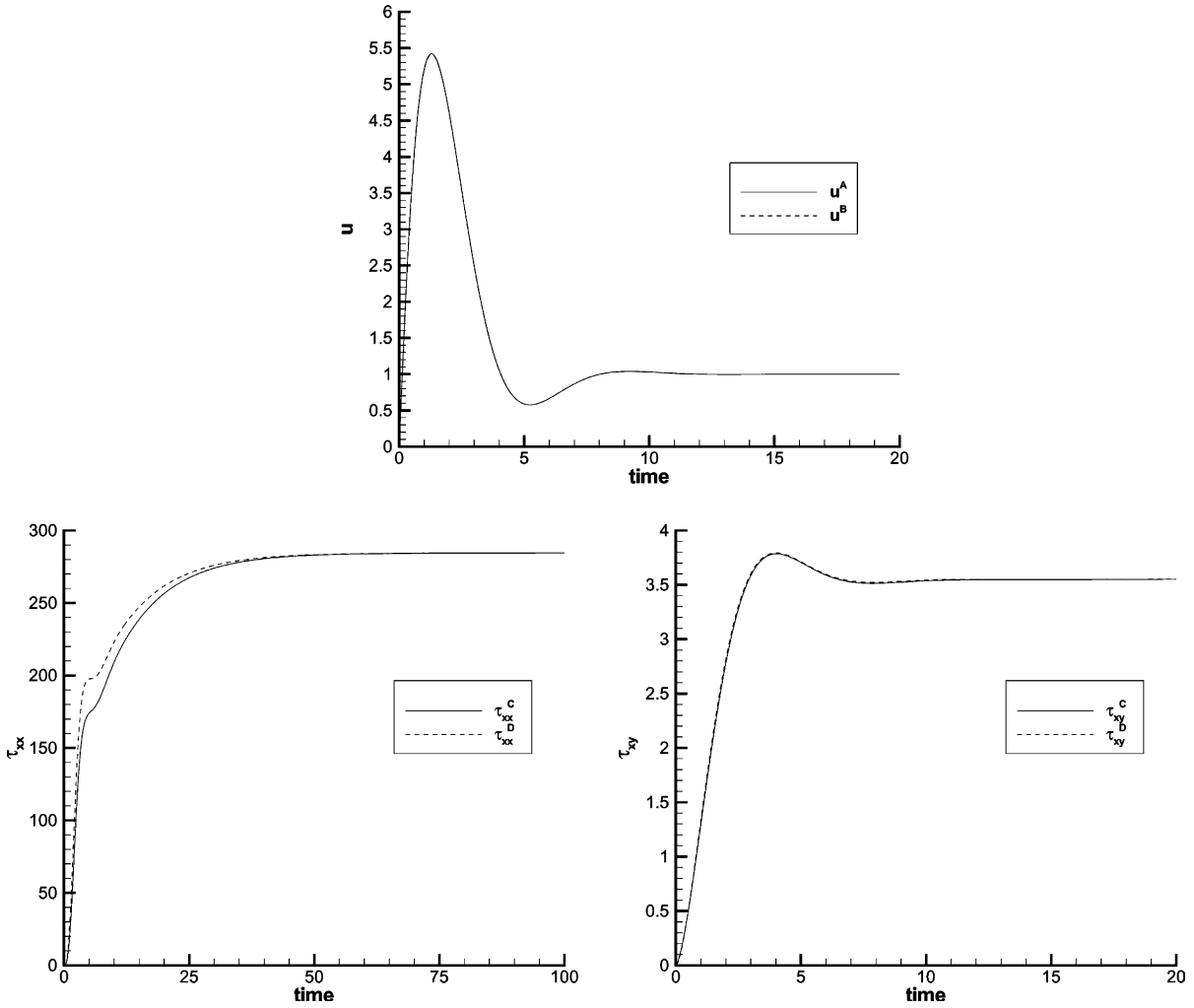

Fig. 9. Transient solution for a channel with $K = 1$ elements, with $N = 4$, for $We = 10$ and $Re = 1$.

seem to play an important role, and negligible difference is observed between the transient numerical solutions shown in Figs. 9 and 10 for $K_y = 1$ and those obtained using $K_y = 4$. The same is true for the comparison of solutions obtained by the first-order Euler/Euler temporal scheme, and the second-order OIFS2/AB2 scheme.

Finally, we comment on alternative implicit schemes for solving this problem. A fully implicit algorithm in which the nonlinear terms were treated iteratively was also implemented. No substantial change in the critical value of the Weissenberg number was observed for either the steady or the transient problem. Fiétier and Deville [8] observed similar behaviour when a fully implicit unsteady solver was used. The problem of spurious oscillations in the solution caused by the inadequate spatial resolution of the continuous spectrum seems to dominate the temporal stability of explicit and implicit schemes to such an extent that the enhanced stability properties one would expect of implicit schemes are imperceptible.

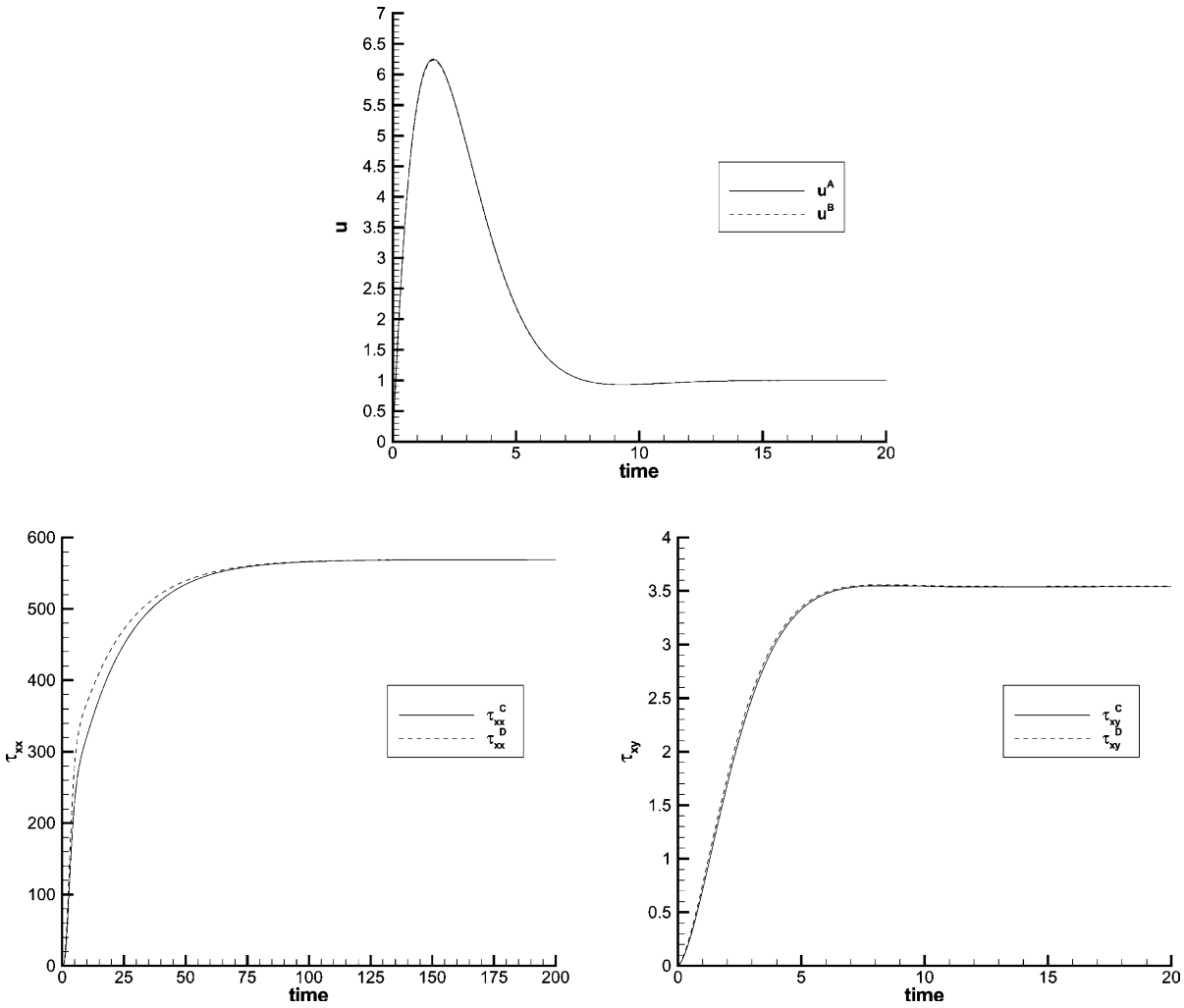

Fig. 10. Transient solution for a channel with $K = 1$ element, with $N = 4$, for $We = 20$ and $Re = 1$.

7. Conclusions

In this paper, steady and transient solutions to the planar Poiseuille flow of Oldroyd B fluids have been calculated and analyzed with respect to stability using a spectral element technique. The spectral element technique developed here incorporates a three-field formulation of the problem in terms of velocity, pressure and extra-stress, a discontinuous extra-stress approximation, a modified continuity equation that ensures that the zero mean condition on pressure is satisfied automatically and a Cahouet–Chabard preconditioner for the Uzawa operator that has been modified for viscoelastic flows. For the transient start-up of plane Poiseuille flow of an Oldroyd B fluid, a comparison has been made between the numerical approximation and the analytical solution of Waters and King [33].

The performance of three different temporal discretization schemes has been compared. When the Oldroyd B model is reduced to the UCM model, by setting $\beta = 0$, the first-order method performs better

than the two second-order methods. The explanation for this may be the regularity of the true solution in time but this is an issue that is currently under investigation. As expected, the numerical solution of the planar Poiseuille flow becomes more stable when the parameter β is increased and when a nonzero Reynolds number is chosen. Increasing the order of the numerical approximation results in a decrease in the critical value of the Weissenberg number. The same behaviour is observed when the length of the channel is shortened, or the number of elements in the lengthwise direction is increased. Increasing the number of elements in the cross channel direction does not influence the stability of the scheme. Apparently, any type of refinement in the lengthwise direction decreases the maximum attainable Weissenber number, whereas this number is insensitive to refinement in the cross channel direction. This is in agreement with the findings of Fiétier and Deville [8].

Acknowledgements

The authors acknowledge many fruitful discussions with members of the Complex Fluids Group at the University of Wales Aberystwyth and, in particular, Professor Russell Davies. We thank one of the referees for their insightful and punctilious reading of the manuscript.

References

[1] K. Atalik, R. Keunings, Non-linear temporal stability analysis of viscoelastic plane channel flow using a fully-spectral method, J. Non-Newtonian Fluid Mech. 102 (2002) 299–319.
[2] D.V. Boger, A highly elastic constant-viscosity fluid, J. Non-Newtonian Fluid Mech. 3 (1977) 87–91.
[3] J. Cahouet, J.P. Chabard, Some fast 3D finite element solvers for the generalized Stokes problem, Int. J. Numer. Meth. Fluid 8 (1988) 869–895.
[4] E.O. Carew, P. Townsend, M.F. Webster, Taylor–Galerkin algorithms for viscoelastic flow: application to a model problem, Num. Meth. Part. Diff. Eqns. 10 (1994) 171–190.
[5] M. Deville, P.F. Fischer, E. Mund, High-order Methods for Incompressible Fluid Flow, Cambridge University Press, Cambridge, 2002.
[6] M. Dryja, O.B. Widlund, Domain decomposition algorithms with small overlap, SIAM J. Sci. Comput. 15 (1994) 604–620.
[7] X. Escriva, E. Leriche, T.N. Phillips, Preconditioned Uzawa algorithm for the velocity–pressure–stress formulation of viscoelastic flow problems, J. Sci. Comput. 17 (2002) 219–229.
[8] N. Fiétier, M.O. Deville, Time-dependent algorithms for the simulation of viscoelastic flows with spectral element methods: application and stability, J. Comput. Phys. 186 (2003) 93–121.
[9] N. Fiétier, Numerical Simulation of Viscoelastic Fluid Flows by Spectral Element Methods and Time-dependent Algorithms, Ph.D. Thesis, Ecole Polytechnique Fédérale de Lausanne, Switzerland, 2002.
[10] P.F. Fischer, An overlapping Schwarz method for spectral element solution of the Navier–Stokes equations, J. Comput. Phys. 133 (1997) 84–101.
[11] M.I. Gerritsma, T.N. Phillips, Discontinuous spectral element approximations for the velocity–pressure–stress formulation of the Stokes problem, Int. J. Numer. Meth. Eng. 43 (1998) 1404–1419.
[12] M.I. Gerritsma, T.N. Phillips, Compatible spectral approximations for the velocity–pressure–stress formulation of the Stokes problem, SIAM J. Sci. Comput. 20 (1999) 1530–1550.
[13] R. Guénette, M. Fortin, A new mixed finite element method for computing viscoelastic flows, J. Non-Newtonian Fluid Mech. 60 (1995) 27–52.
[14] T.C. Ho, M.M. Denn, Stability of plane Poiseuille flow of a highly elastic liquid, J. Non-Newtonian Fluid Mech. 3 (1977/1978) 179–195.
[15] G.E.M. Karniadakis, S.J. Sherwin, Spectral/*hp* Element Methods for CFD, Oxford University Press, Oxford, 1999.
[16] R.A. Keiller, Numerical instability of time-dependent flows, J. Non-Newtonian Fluid Mech. 43 (1992) 229–246.
[17] R.G. Larson, Instabilities in viscoelastic flows, Rheol. Acta 31 (1992) 213–263.
[18] K.C. Lee, B.A. Finlayson, Stability of plane Poiseuille and Couette-flow of a Maxwell fluid, J. Non-Newtonian Fluid Mech. 21 (1986) 65–78.
[19] A. Lozinski, R.G. Owens, An energy estimate for the Oldroyd B model: theory and applications, J. Non-Newtonian Fluid Mech. 112 (2003) 161–176.

[20] Y. Maday, A.T. Patera, E.M. Rønquist, A Well-posed Optimal Spectral Element Approximation for the Stokes Problem, ICASE Report 87-48, Institute for Computer Applications in Science and Engineering, NASA Langley Research Center, Virginia, USA.
[21] Y. Maday, A.T. Patera, Spectral element methods for the incompressible Navier–Stokes equations, in: A.K. Noor, J.T. Oden (Eds.), State of the Art Surveys in Computational Mechanics, ASME, New York, 1989, pp. 71–143.
[22] Y. Maday, A.T. Patera, E.M. Rønquist, An operator-integration-factor splitting method for time-dependent problems: application to incompressible fluid flow, J. Sci. Comput. 5 (1990) 263–292.
[23] J.S. Mullen, P.F. Fischer, Filtering techniques for complex geometry fluid flows, Comm. Numer. Meth. Eng. 15 (1999) 9–18.
[24] R.G. Owens, T.N. Phillips, Computational Rheology, Imperial College Press, London, 2002.
[25] M.G.N. Perera, K. Walters, Long-range memory effects in flows involving abrupt changes in geometry.Part I: Flows associated with L-shaped and T-shaped geometries, J. Non-Newtonian Fluid Mech. 2 (1977) 49–81.
[26] K.C. Porteous, M.M. Denn, Linear stability of plane Poiseuille flow of viscoelastic liquids, Trans. Soc. Rheol. 16 (1972) 295–308.
[27] M. Renardy, W.J. Hrusa, J.A. Nohel, Mathematical problems in viscoelasticity, in: Pitman Monographs and Surveys in Pure and Applied Mathematics, vol. 35, Longman, Harlow, England, 1987.
[28] M. Renardy, Recent advances in the mathematical theory of steady flow of viscoelastic fluids, J. Non-Newtonian Fluid Mech. 29 (1988) 11–24.
[29] M. Renardy, Mathematical analysis of viscoelastic flows, Ann. Rev. Fluid Mech. 21 (1989) 1–36.
[30] M. Renardy, Current issues in non-Newtonian flows: a mathematical perspective, J. Non-Newtonian Fluid Mech. 90 (2000) 243–259.
[31] M.D. Smith, R.C. Armstrong, R.A. Brown, R. Sureshkumar, Finite element analysis of stability of two-dimensional viscoelastic flows to three-dimensional disturbances, J. Non-Newtonian Fluid Mech. 93 (2000) 203–244.
[32] R. Sureshkumar, A.N. Beris, Linear stability analysis of viscoelastic Poiseuille flow using an Arnoldi-based orthogonalization algorithm, J. Non-Newtonian Fluid Mech. 56 (1995) 151–182.
[33] N.D. Waters, M.J. King, Unsteady flow of an elastico-viscous liquid, Rheol. Acta 9 (1970) 345–355.
[34] H.J. Wilson, M. Renardy, Y. Renardy, Structure of the spectrum in zero Reynolds number shear flow of the UCM and Oldroyd B liquids, J. Non-Newtonian Fluid Mech. 80 (1999) 251–268.